Cite as: A. Fichtner *et al.*, *Science* 10.1126/science.adp8094 (2025).

Hidden cascades of seismic ice stream deformation

Andreas Fichtner[1]*, Coen Hofstede[2], Brian L. N. Kennett[3], Anders Svensson[4], Julien Westhoff[4], Fabian Walter[5,6], Jean-Paul Ampuero[7], Eliza Cook[4], Dimitri Zigone[8], Daniela Jansen[2], Olaf Eisen[2,8,9]

[1]Department of Earth and Planetary Sciences, ETH Zurich, Zurich, Switzerland. [2]Alfred-Wegener-Institut Helmholtz-Zentrum für Polar- und Meeresforschung, Bremerhaven, Germany. [3]Research School of Earth Sciences, The Australian National University, Acton, Canberra, Australia. [4]Niels Bohr Institute, University of Copenhagen, Copenhagen, Denmark. [5]Swiss Federal Research Institute WSL, Birmensdorf, Switzerland. [6]Laboratory of Hydraulics, Hydrology and Glaciology VAW, ETH Zurich, Zurich, Switzerland. [7]Université Côte d'Azur, IRD, CNRS, Observatoire de la Côte d'Azur, Geoazur Laboratory, Sophia Antipolis, Valbonne, France. [8]Université de Strasbourg/CNRS, Institut Terre et Environnement de Strasbourg, UMR7063, Strasbourg Cedex, France. [9]Fachbereich Geowissenschaften, Universität Bremen, Bremen, Germany.

***Corresponding author. E-mail: andreas.fichtner@eaps.ethz.ch**

Ice streams are major regulators of sea level change. However, standard viscous flow simulations of their evolution have limited predictive power due to incomplete understanding of involved processes. On the Greenland ice sheet, borehole fiber-optic observations reveal a brittle deformation mode that is incompatible with viscous flow over length scales similar to the resolution of modern ice sheet models: englacial ice quake cascades that are unobservable at the surface. Nucleating near volcanism-related impurities that promote grain boundary cracking, they appear as a macroscopic form of crystal-scale wild plasticity. A conservative estimate indicates that seismic cascades are likely to produce strain rates that are comparable in amplitude to those measured geodetically, thereby providing a plausible missing link between current ice sheet models and observations.

Ice streams strongly affect the total mass balance of the Antarctic and Greenlandic ice sheets (*1*–*3*). The need to predict their behavior in a changing climate and the concomitant consequences for human society motivates the development of ice sheet simulations (*4*). The predictive power of such simulations, e.g., in terms of projected sea level rise, or ice sheet retreat rates is limited by various aspects of existing numerical models, including numerical discretization, and rheology, as well as material, hydraulic and stress-strain conditions at the base (*3*, *5*, *6*). To date, however, knowledge of model boundary conditions and rheology is largely limited by the difficulty to perform in situ measurements of glacial properties and processes. Here, we employ Distributed Acoustic Sensing (DAS) (*7*, *8*) to detect a mode of ice deformation, which cannot be reconciled with the commonly used non-linear viscous rheology of Glen's flow law (*9*): cascading englacial thrust faulting, observed near the borehole of the East Greenland Ice Core Project (EastGRIP) on the Northeast Greenland Ice Stream (NEGIS) (Fig. 1, A and B). Accounting for ~12% of its total mass discharge (*1*, *10*), NEGIS is the largest ice stream of the Greenland Ice Sheet and a major contributor to current sea level rise (*2*), which underlines the importance of understanding its rheology and deformation mechanisms. In this context, ice core crystallography at EastGRIP has been studied extensively employing both in-situ observations (*11*) and remote geophysical methods (*12*), e.g., to link variations in crystal orientation to large-scale viscous flow patterns (*13*). Optical line scanning has produced images of structures very similar to geological fault-bend folds on thrust ramps, a type of thrust structure (*14*) (Fig. 1C) that have not been observed in ice cores before (*15*). While they evidence that shortening was accommodated by brittle deformation structures in the past, their current activity and contribution to ice deformation remain elusive.

As illustrated in Fig. 1B, we lowered a loose-tube fiber-optic cable, containing four single-mode fibers, 1500 m into the EastGRIP borehole, which had reached a depth of 2420 m at that time. For 14 hours, on 10 August 2022, we measured longitudinal strain rate along the cable using a Silixa iDAS v2 interrogator with 10 m gauge length. Thanks to an average borehole inclination of ~3°, the cable was frictionally coupled to the borehole wall, thereby providing high-quality recordings of seismic body waves, originating from active-shot experiments (*16*). In addition to these, the DAS cable recorded a large variety of natural englacial seismicity, including small individual events, as well as event cascades that lasted for several seconds.

Phenomenology

The borehole DAS recordings from 10 August 2022 contain five clear seismic event sequences, possibly representing the dynamic process behind the brittle deformation patterns observed in the EastGRIP ice core. A visual summary of the sequences is shown in Figs. 2 and 3. This is complemented by a more comprehensive data survey in figs. S1 to S4. To tie borehole depth to age, we use the EastGRIP ice chronology of (*17*). Such conversions are indicated by ka b2k, which uses the year 2000 AD as origin.

The sequences, with one to more than 100 subevents, have several characteristic properties. Most obviously, all

subevents have a radiation pattern that is antisymmetric in the vertical direction, regardless of their amplitude and location. The subevents generally start with positive strain rates (extension in fiber direction) radiating up- and negative strain rates (shortening in fiber direction) radiating downwards. The character of many of the subevents resembles plane waves with apparent wave speeds ranging from 2000–3000 m/s, which is significantly faster than the S wave speed (~1800 m/s) but slower than the P wave speed (~3800 m/s) in the ice around EastGRIP (*16*). Thus they are oblique S waves. Within layers of 10–20 m thickness, we observe shortening that lasts up to tens of seconds (e.g., Fig. 2A, iii) and may be interpreted as creep. These deforming layers seem to temporarily impede the upward propagation of the wave field and in some cases lead to strong downward reflections with a reflection coefficient of around 0.5 (e.g., Figs. 2, A, ii, and B, v).

Despite their complexity, the initial high-amplitude parts of sequences 2 and 5 are remarkably similar. (Fig. 3C). They are composed of an upward-migrating cascade of subevents that originate at identical depths in both sequences. While each subevent of a cascade radiates a wave field downwards, the upward radiation stops after few tens of meters at a layer where creep occurs for 10–50 ms, before the next subevent initiates.

As detailed in supplementary section S2, none of the sequences observed in the EastGRIP borehole was detected by the geophone array at the surface, with the closest geophone installed at a distance of 160 m from the borehole. This lack of surface observability is consistent with the DAS data, which do not show wave propagation extending beyond the thin creeping layers, and explains the absence of similar observations in the literature. Although weak seismic reflectors have been mapped below EastGRIP (*16*), comparable strong reflections off the creeping layers as, e.g., in subevents 1.ii and 2.v, are not present in active-shot data recorded with DAS in the borehole (*16*), and shown in supplement 3.1. This result excludes known changes in fabric orientation (*12*) as the cause for these reflections. The depths of the creeping layers marked with $*$ and + in Fig. 2 coincide with the depth of two tephra (glass component of volcanic ash) layers that were identified in the EastGRIP ice core: the Mt. Mazama (Crater Lake, U.S.) tephra dated at 7.6 ka b2k and the Saksunarvatn (Grimsvötn, Iceland) tephra dated at 10.2 ka b2k. (See section S3.2 for details.) In a similar context, we observe that many of the subevents in sequences 2 and 5 (Fig. 3c) initiate near depths where SO_4 spikes, caused by volcanic eruptions, have been inferred from a projection of GRIP2 sulfate measurements onto the EastGRIP depth scale. (See section S3.3 for details.) Numerous subevents, especially in sequences 1, 3 and 4, initiate at 1360 m depth, close to the abrupt transition around 14.7 ka b2k from the cold climate of the Oldest Dryas/GS-2 stadial to the milder Bølling-Allerød/GI-1 climatic period. Located at 1375 m depth, this transition is particularly sharp at EastGRIP and manifests itself by increasing ice crystal sizes (*18*) in response to decreasing impurity (e.g., dust particle) content by a factor of 10 to 100 (*19*). The end of the Bølling-Allerød/GI-1 at 12.9 ka b2k or 1284 m depth is close to the creeping layer in Fig. 2A, iii, and the occurrence of downward reflections in Fig. 2A, ii. It is preceded by a ~110-year cluster of elevated global volcanic activity that manifests itself in a dense series of SO_4 spikes in Greenland ice cores (*20*, *21*). Abrupt changes in crystallographic fabric orientation are not detectable at any of these depths, neither in ice-core observations nor radar-based inferences (*12*). We therefore exclude changes in fabric as a dominating contributor to the observed nucleation locations.

Source mechanisms and wave field simulations

We can also exclude that the events are cable waves, which are nearly monochromatic oscillations or travelling waves reflecting off the cable end (*22*, *23*) that we do not observe. Furthermore, sequences 2 and 5 seem to initiate below 1500 m depth, and sequence 1 seems to propagate beyond 1500 m depth without evidence for upward reflections off the cable end. Correlations of initiation depths with SO_4 content and tephra layers, as well as variable apparent wave speeds, make it even less likely that our observations are cable waves.

Using the approach detailed in section S4, we derive general source characteristics of the event sequences that explain key features listed above. The observed antisymmetric radiation pattern in the vertical direction constrains the range of possible fault orientations. In a cylindrical coordinate system, where r denotes distance to borehole axis, z depth and ϕ azimuth, the diagonal moment tensor components, M_{rr}, $M_{\phi\phi}$ and M_{zz} produce symmetric radiation patterns and therefore can be excluded, as explained in section S4.1. Wave fields excited by moment tensor components $M_{r\phi}$ and $M_{z\phi}$ cannot be observed with our experimental geometry. This implies that the sources must have a nonzero M_{rz} component, corresponding to either radially directed slip on a horizontal fault or vertically directed slip on a vertical fault. Furthermore, the source location must be at some distance from the cable because an M_{rz}-component source directly at the cable would not be observable. In summary, the data require the absence of an isotropic (explosive/implosive) component but are unable to constrain the precise orientation of the slip plane. Since brittle slip is likely to occur along pre-existing horizontal layers within the ice sheet, we continue to model the seismic sources as slip on a horizontal plane.

The vertically cascading sequences 2 and 5 hint at a generation mechanism of plane waves with variable apparent wave speeds, as recorded by the DAS system. As explained quantitatively in section S4.2.1. and illustrated schematically

in Fig. 4A, a linear array of approximately vertically-aligned horizontal fault planes that are triggered successively produces plane waves with an apparent wave speed controlled by the triggering speed and the inclination angle. Apparent wave speeds above the S wave speed can result from tilting the array toward the DAS cable and/or from P wave triggering, previously observed for earthquakes (*24*). Successive excitation of ruptures on horizontal fault planes already allows us to explain less complex parts of the recordings, such as subevent 1.i and sequence 3, shown in Fig. 4, B and C. In these, and all subsequent simulations, sources at distances between 10–50 m from the borehole produce synthetic strain rate data that are compatible with the observations.

Large subevents in sequences 1, 2 and 5 cause creep that lasts up to several tens of seconds within thin layers, which produce strong reflections that are not present in the active surface shot data (*16*). The presence of such reflections may be explained by temporary fracturing or unwelding of an internal interface, as illustrated schematically in Fig. 5A. In contrast to welded interfaces (*25*), nonwelded interfaces generate reflections and impede transmission in the absence of a material impedance contrast (*26*, *27*). In the idealized case of a planar interface, detailed in section S4.3, reflection and transmission coefficients can be derived analytically. The results indicate that a specific compliance of the interfaces on the order of 10^{-9} to 10^{-8} m/Pa can explain observed reflections off the strain accumulation layers and the resulting absence of surface observations of the event sequences. Less idealized distributions of nonwelded interfaces effectively behave as anisotropic layers, with reflection and transmission controlled by geometric properties of the fractures, including their orientation and density (*28*, *29*). As illustrated in Fig. 5B, a reflector at 1290 m depth, allows us to simulate the more complex event sequence 1.ii, consisting of at least 5 distinguishable subevents, some of which produce clearly visible reflections. Similarly, Fig. 5C shows two subevents from sequence 2.ii, simulated with reflectors at 1050 and 1025 m depth. Millimeter- to centimeter-scale fractures in ice have healing times on the order of tens to hundreds of seconds (*30*), consistent with our observation that active-shots data obtained several minutes after the natural events do not feature similar strong reflections.

Moment magnitudes estimated from DAS recordings of vertical strain ε_{zz} range from $M_w = -2.3$ for the foreshock 1.i to $M_w = -0.24$ for the following main shock sequence 1.ii. They constrain the shear strain ε_{xz} accumulated by a seismic cascade. As detailed in section S5, only ~10% of actual strain were transferred into the fiber, meaning that estimated magnitudes are too low by ~0.67. Magnitude uncertainties are around ±0.5, primarily originating from uncertainties in the distance of the events from the cable and the inability to constrain $M_{r\varphi}$ and $M_{z\varphi}$. The characteristic rupture size L can be deduced from M_w. Assuming that the stress drop $\Delta\sigma$ is 10 % of typical ice stream driving stresses of 100 kPa (*31*), the circular-fault model $L = (7M_0/16\Delta\sigma)^{1/3}$ (*32*) yields rupture sizes on the order of 1 to 10 m for our M_0 estimates between $\sim 3 \cdot 10^5$ and $\sim 2 \cdot 10^8$ Nm. The application of Hooke's law, $\Delta\sigma = \mu D/L$, with shear modulus $\mu \approx 2.8 \cdot 10^9$ gives rupture displacements D on the order of tens to hundreds of micrometers. Applied to an individual event of sequence 2.i (Fig. 5C), and taking the uncertainty in the moment estimate into account, this analysis yields D between $5 \cdot 10^{-5}$ and $2 \cdot 10^{-4}$ m per subevent. With $N \approx 50$ subevents spread over a depth range of $Z \approx 600$ m, a cascade like 2.i accumulates an average shear strain $\varepsilon_{xz} = ND/Z$ on the order of $3 \cdot 10^{-6}$ to $2 \cdot 10^{-5}$ m/m. A critical component of these estimates is the stress drop, which has a typical uncertainty of a factor of 10 for well-observed earthquakes (*33*). Adopting this uncertainty estimate for our case, expands the range of ε_{xz} to $1 \cdot 10^{-6}$ to $8 \cdot 10^{-5}$ m/m.

Implications for ice stream dynamics

Relevance for ice stream deformation

As detailed in section S6, cascading englacial ice quakes cannot result from the presence of the borehole. However, the characteristics of the events are not typical for glacial microseismicity, which is mostly associated with shear and tensile faulting near the surface and at the bed (*34*). Reported englacial icequakes beneath the surface crevasse zone have tensile source mechanisms (*35*), in contrast to the events observed here. Tremor-like shear rupturing was located at the ice bed (*36*). Hence, cascading brittle failure within the ice may be particular to ice streams, where a vertical girdle crystallographic fabric forms to accommodate longitudinal extension (*37*, *38*). The resulting anisotropy causes significant hardening in the along-flow direction (*13*), which may result in brittle failure when stresses are sufficiently high.

The most conservative estimate of strain induced by the large cascade 2.i, $\varepsilon_{xz} = 10^{-6}$ m/m, implies that around 100 of these event cascades may locally produce deformation that is comparable in amplitude to the 10^{-4} m/m horizontal strain per year inferred from GPS measurements around EastGRIP (*39*). Although the relevance of englacial seismicity for large-scale ice stream deformation depends on its spatio-temporal distribution, the fact that we observe two large cascades within only 14 hours suggests that the phenomenon occurs rather frequently.

A similar long-term extrapolation can be made for the creeping deformation within thin layers. The largest-amplitude sequence 1.ii, for example, has average strain rates of $\sim 5 \cdot 10^{-7}$ m/m/s lasting for ~0.1 s. Taking into account that only ~10% of the actual strain is transmitted into the fiber (see section S5), we find that around 100 such events yield vertical strain rates that are also on the order of 10^{-4} yr^{-1}. However, without knowing the exact deformation style, an

estimation of the corresponding horizontal strain is not possible.

At this stage, we may only speculate about the spatial distribution of seismic cascades. Radar sounding (*40*) and surface velocity observations (*41*) show that the internal ice structure and kinematics hardly vary over tens of kilometers around EastGRIP. The observed englacial seismicity is therefore unlikely to be a local peculiarity caused by local flow anomalies but instead typical for the regional ice flow pattern. In summary, it seems plausible that seismic cascades are a common phenomenon in ice streams, but follow-up investigations are necessary for it to be confidently included in or excluded from ice sheet simulations.

Bridging scales: From laboratory experiments to ice stream dynamics

Englacial seismic cascades near EastGRIP suggest that various properties and phenomena observed in laboratory experiments extrapolate to larger scales. Laboratory tests on mono- and polycrystalline ice show a distinct SO_4-induced reduction in viscosity resulting from increased dislocation density (*42*) and enhanced mico-cracking along grain boundaries (*43*). Near EastGRIP, these weaknesses promote creep over tens of μs, the nucleation of seismic events and their vertical cascading over more than 600 m. Seismic cascades do not require the presence of pronounced tephra layers, which have not been observed near the large majority of SO_4 peaks. However, when tephra with grain sizes in the tens of μm range, compared to the μm-scale of background dust (*44*), is present, it promotes creep over tens of seconds in thin layers and temporary unwelding that impedes the upward propagation of seismic waves. The underlying crystal-scale process may be impurity-induced grain-size reduction that causes the deformation mechanism to switch to grain-boundary sliding, known to enhance creep (*45*, *46*). Direct observations of cracks and deformation-related structures are, however, challenging. Centimeter-scale fractures heal over time scales of minutes (*30*), and ice core samples are too small and too remote from the inferred location of the seismic cascades to provide constraints.

Experiments on single ice crystals have revealed dislocation avalanches that manifest themselves as long-term plasticity (*47*). These avalanches can trigger deformation cascades across grains that are hypothesized to be limited only by the laboratory system size (*48*). Our observations suggest that these microscopic cascades extend to ruptures at the tens of centimeter to meter scale, which then trigger macroscopic seismic cascades across hundreds of meters. When averaged over large enough distances, this deformation style may still produce a smooth stress-strain curve, thereby defining a representative volume element (RVE) for effective viscous deformation. Hence, our observation of seismic cascades propagating over at least 600 m implies that the RVE of ice stream ice is not at the centimeter but at the kilometer scale.

A plausible missing link: Implications for ice sheet modeling and future research

Our results imply that Glen's flow law for polycrystalline ice (*49*) is not applicable to ice stream modeling at spatial scales close to or smaller than the kilometer-size RVE. This flow law describes secondary creep over time scales longer than the Maxwell time, which itself is orders of magnitude longer than the seismogenic failure of the large-amplitude sequence 1.ii (*34*). Moreover, Glen's flow law is rate strengthening, whereas a rate weakening rheology is necessary to produce dynamic instability during seismogenic deformation (*50*).

The magnitude of observed englacial seismicity suggests it as a plausible missing link between observed surface velocities in the upstream part of NEGIS and the results of current ice sheet models, which still fail to adequately reproduce the geometry and extent of NEGIS with the commonly used flow-law exponent of $n = 3$ (*51*, *52*).

At scales exceeding the RVE, the observed seismic deformation may be a process that contributes to the macroscopic effect of a larger exponent around $n = 4$, recently proposed for fast-flowing regions of the Greenland and Antarctic ice sheets (*53*–*55*). However, to accurately model narrow ice streams, numerical resolutions as low as few hundred meters are needed (*56*, *57*), thereby moving the grid spacing below the size of the RVE. Consequently, the impact of cascading seismicity on ice stream deformation should be considered to ensure reliable predictions of ice mass loss and sea level rise. This will require additional and longer borehole DAS experiments to better constrain the spatio-temporal distribution of the phenomenon, investigations on underlying crystal-scale processes, and modelling studies that constrain the interplay between englacial seismicity, rheology and large-scale flow patterns.

REFERENCES AND NOTES

1. S. A. Khan, K. H. Kjær, M. Bevis, J. L. Bamber, J. Wahr, K. K. Kjeldsen, A. A. Bjørk, N. J. Korsgaard, L. A. Stearns, M. R. van den Broeke, L. Liu, N. K. Larsen, I. S. Muresan, Sustained mass loss of the northeast Greenland ice sheet triggered by regional warming. *Nat. Clim. Chang.* **4**, 292–299 (2014). doi:10.1038/nclimate2161
2. M. D. King, I. M. Howat, S. G. Candela, M. J. Noh, S. Jeong, B. P. Y. Noël, M. R. van den Broeke, B. Wouters, A. Negrete, Dynamic ice loss from the Greenland Ice Sheet driven by sustained glacier retreat. *Commun. Earth Environ.* **1**, 1 (2020). doi:10.1038/s43247-020-0001-2
3. H. Seroussi, V. Verjans, S. Nowicki, A. J. Payne, H. Goelzer, W. H. Lipscomb, A. Abe-Ouchi, C. Agosta, T. Albrecht, X. Asay-Davis, A. Barthel, R. Calov, R. Cullather, C. Dumas, B. K. Galton-Fenzi, R. Gladstone, N. R. Golledge, J. M. Gregory, R. Greve, T. Hattermann, M. J. Hoffman, A. Humbert, P. Huybrechts, N. C. Jourdain, T. Kleiner, E. Larour, G. R. Leguy, D. P. Lowry, C. M. Little, M. Morlighem, F. Pattyn, T. Pelle, S. F. Price, A. Quiquet, R. Reese, N.-J. Schlegel, A. Shepherd, E. Simon, R. S. Smith, F. Straneo, S. Sun, L. D. Trusel, J. Van Breedam, P. Van Katwyk, R. S. W. van de Wal, R. Winkelmann, C. Zhao, T. Zhang, T. Zwinger, Insights into the vulnerability of Antarctic glaciers from the ISMIP6 ice sheet model ensemble and

associated uncertainty. *Cryosphere* **17**, 5197–5217 (2023). doi:10.5194/tc-17-5197-2023
4. J. A. Church *et al*., *Climate Change 2013: The Physical Science Basis. Contribution of Working Group I to the Fifth Assessment Report of the Intergovernmental Panel on Climate Change* (Cambridge University Press, 2013).
5. C. Ritz, T. L. Edwards, G. Durand, A. J. Payne, V. Peyaud, R. C. A. Hindmarsh, Potential sea-level rise from Antarctic ice-sheet instability constrained by observations. *Nature* **528**, 115–118 (2015). doi:10.1038/nature16147 Medline
6. I. Joughin, B. E. Smith, C. G. Schoof, Regularized Coulomb Friction Laws for Ice Sheet Sliding: Application to Pine Island Glacier, Antarctica. *Geophys. Res. Lett.* **46**, 4764–4771 (2019). doi:10.1029/2019GL082526 Medline
7. A. Hartog, *An introduction to distributed optical fibre sensors* (CRC Press, 2017).
8. N. J. Lindsey, E. Martin, Fiber-Optic Seismology. *Annu. Rev. Earth Planet. Sci.* **49**, 309–336 (2021). doi:10.1146/annurev-earth-072420-065213
9. R. Greve, H. Blatter, *Dynamics of Ice Sheets and Glaciers* (Springer, 2009).
10. E. Rignot, J. Mouginot, Ice flow in Greenland for the International Polar Year 2008–2009. *Geophys. Res. Lett.* **39**, 2012GL051634 (2012). doi:10.1029/2012GL051634
11. N. J. Stoll, J. Eichler, M. Hörhold, T. Erhardt, C. Jensen, I. Weikusat, Microstructure, micro-inclusions, and mineralogy along the EGRIP ice core – Part 1: Localisation of inclusions and deformation patterns. *Cryosphere* **15**, 5717–5737 (2021). doi:10.5194/tc-15-5717-2021
12. O. Zeising, T. A. Gerber, O. Eisen, M. R. Ershadi, N. Stoll, I. Weikusat, A. Humbert, Improved estimation of the bulk ice crystal fabric asymmetry from polarimetric phase co-registration. *Cryosphere* **17**, 1097–1105 (2023). doi:10.5194/tc-17-1097-2023
13. T. A. Gerber, D. A. Lilien, N. M. Rathmann, S. Franke, T. J. Young, F. Valero-Delgado, M. R. Ershadi, R. Drews, O. Zeising, A. Humbert, N. Stoll, I. Weikusat, A. Grinsted, C. S. Hvidberg, D. Jansen, H. Miller, V. Helm, D. Steinhage, C. O'Neill, J. Paden, S. P. Gogineni, D. Dahl-Jensen, O. Eisen, Crystal orientation fabric anisotropy causes directional hardening of the Northeast Greenland Ice Stream. *Nat. Commun.* **14**, 2653 (2023). doi:10.1038/s41467-023-38139-8 Medline
14. K. R. McClay, Ed., *Thrust Tectonics* (Chapman & Hall, 1992), pp. 419–433.
15. J. Westhoff, Visual stratigraphy of the EastGRIP ice core, PhD thesis, University of Copenhagen, Niels Bohr Institute (2021).
16. A. Fichtner, C. Hofstede, L. Gebraad, A. Zunino, D. Zigone, O. Eisen, Borehole fibre-optic seismology inside the Northeast Greenland Ice Stream. *Geophys. J. Int.* **235**, 2430–2441 (2023). doi:10.1093/gji/ggad344
17. S. Mojtabavi, F. Wilhelms, E. Cook, S. M. Davies, G. Sinnl, M. Skov Jensen, D. Dahl-Jensen, A. Svensson, B. M. Vinther, S. Kipfstuhl, G. Jones, N. B. Karlsson, S. H. Faria, V. Gkinis, H. A. Kjær, T. Erhardt, S. M. P. Berben, K. H. Nisancioglu, I. Koldtoft, S. O. Rasmussen, A first chronology for the East Greenland Ice-core Project (EGRIP) over the Holocene and last glacial termination. *Clim. Past* **16**, 2359–2380 (2020). doi:10.5194/cp-16-2359-2020
18. N. J. Stoll, J. Westhoff, P. Bohleber, A. Svensson, D. Dahl-Jensen, C. Barbante, I. Weikusat, Chemical and visual characterisation of EGRIP glacial ice and cloudy bands within. *Cryosphere* **17**, 2021–2043 (2023). doi:10.5194/tc-17-2021-2023
19. S. Schüpbach, H. Fischer, M. Bigler, T. Erhardt, G. Gfeller, D. Leuenberger, O. Mini, R. Mulvaney, N. J. Abram, L. Fleet, M. M. Frey, E. Thomas, A. Svensson, D. Dahl-Jensen, E. Kettner, H. Kjaer, I. Seierstad, J. P. Steffensen, S. O. Rasmussen, P. Vallelonga, M. Winstrup, A. Wegner, B. Twarloh, K. Wolff, K. Schmidt, K. Goto-Azuma, T. Kuramoto, M. Hirabayashi, J. Uetake, J. Zheng, J. Bourgeois, D. Fisher, D. Zhiheng, C. Xiao, M. Legrand, A. Spolaor, J. Gabrieli, C. Barbante, J.-H. Kang, S. D. Hur, S. B. Hong, H. J. Hwang, S. Hong, M. Hansson, Y. Iizuka, I. Oyabu, R. Muscheler, F. Adolphi, O. Maselli, J. McConnell, E. W. Wolff, Greenland records of aerosol source and atmospheric lifetime changes from the Eemian to the Holocene. *Nat. Commun.* **9**, 1476 (2018). doi:10.1038/s41467-018-03924-3 Medline
20. A. Svensson, D. Dahl-Jensen, J. P. Steffensen, T. Blunier, S. O. Rasmussen, B. M. Vinther, P. Vallelonga, E. Capron, V. Gkinis, E. Cook, H. A. Kjær, R. Muscheler, S. Kipfstuhl, F. Wilhelms, T. F. Stocker, H. Fischer, F. Adolphi, T. Erhardt, M. Sigl, A. Landais, F. Parrenin, C. Buizert, J. R. McConnell, M. Severi, R. Mulvaney, M. Bigler, Bipolar volcanic synchronization of abrupt climate change in Greenland and Antarctic ice cores during the last glacial period. *Clim. Past* **16**, 1565–1580 (2020). doi:10.5194/cp-16-1565-2020
21. P. M. Abbott, U. Niemeier, C. Timmreck, F. Riede, J. R. McConnell, M. Severi, H. Fischer, A. Svensson, M. Toohey, F. Reinig, M. Sigl, Volcanic climate forcing preceding the inception of the Younger Dryas: Implications for tracing the Laacher See eruption. *Quat. Sci. Rev.* **274**, 107260 (2021). doi:10.1016/j.quascirev.2021.107260
22. J. D. Munn, T. I. Coleman, B. L. Parker, M. J. Mondanos, A. Chalari, Novel cable coupling technique for improved shallow distributed acoustic sensor VSPs. *J. Appl. Geophys.* **138**, 72–79 (2017). doi:10.1016/j.jappgeo.2017.01.007
23. D. Mata Flores, E. D. Mercerat, J. P. Ampuero, D. Rivet, A. Sladen, Identification of two vibration regimes of underwater fibre optic cables by distributed acoustic sensing. *Geophys. J. Int.* **234**, 1389–1400 (2023). doi:10.1093/gji/ggad139
24. M. Vallée, Y. Xie, R. Grandin, J. C. Villegas-Lanza, J.-M. Nocquet, S. Vaca, L. Meng, J. P. Ampuero, P. Mothes, P. Jarrin, C. Sierra Farfán, F. Rolandone, Self-reactivated rupture during the 2019 M = 8 northern Peru intraslab earthquake. *Earth Planet. Sci. Lett.* **601**, 117886 (2023). doi:10.1016/j.epsl.2022.117886
25. K. Aki, P. Richards, *Quantitative Seismology* (University Science Books, 2002).
26. M. Schoenberg, Elastic wave behavior across linear slip interfaces. *J. Acoust. Soc. Am.* **68**, 1516–1521 (1980). doi:10.1121/1.385077
27. E. S. Krebes, *J. Canadian Soc. Expl. Geophys.* **23**, 66 (1987).
28. E. Liu, J. A. Hudson, T. Pointer, Equivalent medium representation of fractured rock. *J. Geophys. Res.* **105** (B2), 2981–3000 (2000). doi:10.1029/1999JB900306
29. S. Jin, A. Stovas, Exact and approximate reflection/transmission responses from a layer containing vertical fractures. *Geophys. J. Int.* **222**, 260–288 (2020). doi:10.1093/gji/ggaa162
30. A. Murdza, E. M. Schulson, C. E. Renshaw, A. Polojärvi, Rapid Healing of Thermal Cracks in Ice. *Geophys. Res. Lett.* **49**, e2022GL099771 (2022). doi:10.1029/2022GL099771
31. O. V. Sergienko, T. T. Creyts, R. C. A. Hindmarsh, Similarity of organized patterns in driving and basal stresses of Antarctic and Greenland ice sheets beneath extensive areas of basal sliding. *Geophys. Res. Lett.* **41**, 3925–3932 (2014). doi:10.1002/2014GL059976
32. H. Kanamoori, D. L. Anderson, *Bull. Seismol. Soc. Am.* **65**, 1073 (1975).
33. R. E. Abercrombie, Resolution and uncertainties in estimates of earthquake stress drop and energy release. *Philos. Trans. A Math. Phys. Eng. Sci.* **379**, 20200131 (2021). doi:10.1098/rsta.2020.0131 Medline
34. E. A. Podolskiy, F. Walter, Cryoseismology. *Rev. Geophys.* **54**, 708–758 (2016). doi:10.1002/2016RG000526
35. F. Walter, J. F. Clinton, N. Deichmann, D. S. Dreger, S. E. Minson, M. Funk, Moment Tensor Inversions of Icequakes on Gornergletscher, Switzerland. *Bull. Seismol. Soc. Am.* **99** (2A), 852–870 (2009). doi:10.1785/0120080110
36. J. Umlauft, F. Lindner, P. Roux, T. D. Mikesell, M. M. Haney, M. Korn, F. T. Walter, Stick-Slip Tremor Beneath an Alpine Glacier. *Geophys. Res. Lett.* **48**, e2020GL090528 (2021). doi:10.1029/2020GL090528
37. D. H. Richards, S. S. Pegler, S. Piazolo, N. Stoll, I. Weikusat, Bridging the Gap Between Experimental and Natural Fabrics: Modeling Ice Stream Fabric Evolution and its Comparison With Ice-Core Data. *J. Geophys. Res. Solid Earth* **128**, e2023JB027245 (2023). doi:10.1029/2023JB027245
38. D. A. Lilien, N. M. Rathmann, C. S. Hvidberg, D. Dahl-Jensen, Modeling Ice-Crystal Fabric as a Proxy for Ice-Stream Stability. *J. Geophys. Res. Earth Surf.* **126**, e2021JF006306 (2021). doi:10.1029/2021JF006306
39. C. S. Hvidberg, A. Grinsted, D. Dahl-Jensen, S. A. Khan, A. Kusk, J. K. Andersen, N. Neckel, A. Solgaard, N. B. Karlsson, H. A. Kjær, P. Vallelonga, Surface velocity of the Northeast Greenland Ice Stream (NEGIS): Assessment of interior velocities derived from satellite data by GPS. *Cryosphere* **14**, 3487–3502 (2020). doi:10.5194/tc-14-3487-2020
40. S. Franke, D. Jansen, T. Binder, J. D. Paden, N. Dörr, T. A. Gerber, H. Miller, D. Dahl-Jensen, V. Helm, D. Steinhage, I. Weikusat, F. Wilhelms, O. Eisen, Airborne ultra-wideband radar sounding over the shear margins and along flow lines at the onset region of the Northeast Greenland Ice Stream. *Earth Syst. Sci. Data* **14**, 763–779 (2022). doi:10.5194/essd-14-763-2022
41. I. Joughin, B. E. Smith, I. M. Howat, A complete map of Greenland ice velocity derived from satellite data collected over 20 years. *J. Glaciol.* **64**, 1–11 (2018). doi:10.1017/jog.2017.73 Medline

42. Y. L. Trickett, I. Baker, P. M. S. Pradhan, The effects of sulfuric acid on the mechanical properties of ice single crystals. *J. Glaciol.* **46**, 239–243 (2000). doi:10.3189/172756500781832819
43. K. Hammonds, I. Baker, The Effects of H_2SO_4 on the Mechanical Behavior and Microstructural Evolution of Polycrystalline Ice. *J. Geophys. Res. Earth Surf.* **123**, 535–556 (2018). doi:10.1002/2017JF004335
44. J. P. Steffensen, The size distribution of microparticles from selected segments of the Greenland Ice Core Project ice core representing different climatic periods. *J. Geophys. Res.* **102** (C12), 26755–26763 (1997). doi:10.1029/97JC01490
45. D. L. Goldsby, D. L. Kohlstedt, Superplastic deformation of ice: Experimental observations. *J. Geophys. Res.* **106** (B6), 11017–11030 (2001). doi:10.1029/2000JB900336
46. M. D. Behn, D. L. Goldsby, G. Hirth, The role of grain size evolution in the rheology of ice: Implications for reconciling laboratory creep data and the Glen flow law. *Cryosphere* **15**, 4589–4605 (2021). doi:10.5194/tc-15-4589-2021
47. J. Weiss, J. R. Grasso, Acoustic Emission in Single Crystals of Ice. *J. Phys. Chem. B* **101**, 6113–6117 (1997). doi:10.1021/jp963157f
48. J. Weiss, Ice: The paradigm of wild plasticity. *Philos. Trans. A Math. Phys. Eng. Sci.* **377**, 20180260 (2019). doi:10.1098/rsta.2018.0260 Medline
49. E. M. Schulson, P. Duval, *Creep and fracture of ice* (Cambridge University Press, 2009).
50. C. H. Scholz, Earthquakes and friction laws. *Nature* **391**, 37–42 (1998). doi:10.1038/34097
51. A. Aschwanden, M. A. Fahnestock, M. Truffer, Complex Greenland outlet glacier flow captured. *Nat. Commun.* **7**, 10524 (2016). doi:10.1038/ncomms10524 Medline
52. M. Rückamp, R. Greve, A. Humbert, Comparative simulations of the evolution of the Greenland ice sheet under simplified Paris Agreement scenarios with the models SICOPOLIS and ISSM. *Polar Sci.* **21**, 14–25 (2019). doi:10.1016/j.polar.2018.12.003
53. F. Gillet-Chaulet, R. C. A. Hindmarsh, H. F. J. Corr, E. C. King, A. Jenkins, *In-situ* quantification of ice rheology and direct measurement of the Raymond Effect at Summit, Greenland using a phase-sensitive radar. *Geophys. Res. Lett.* **38**, n/a (2011). doi:10.1029/2011GL049843
54. P. D. Bons, T. Kleiner, M.-G. Llorens, D. J. Prior, T. Sachau, I. Weikusat, D. Jansen, Greenland Ice Sheet: Higher Nonlinearity of Ice Flow Significantly Reduces Estimated Basal Motion. *Geophys. Res. Lett.* **45**, 6542–6548 (2018). doi:10.1029/2018GL078356
55. J. D. Millstein, B. M. Minchew, S. S. Pegler, Ice viscosity is more sensitive to stress than commonly assumed. *Commun. Earth Environ.* **3**, 57 (2022). doi:10.1038/s43247-022-00385-x
56. E. Bueler, Stable finite volume element schemes for the shallow-ice approximation. *J. Glaciol.* **62**, 230–242 (2016). doi:10.1017/jog.2015.3
57. A. Aschwanden, M. A. Fahnestock, M. Truffer, D. J. Brinkerhoff, R. Hock, C. Khroulev, R. Mottram, S. A. Khan, Contribution of the Greenland Ice Sheet to sea level over the next millennium. *Sci. Adv.* **5**, eaav9396 (2019). doi:10.1126/sciadv.aav9396 Medline
58. P. Vallelonga, K. Christianson, R. B. Alley, S. Anandakrishnan, J. E. M. Christian, D. Dahl-Jensen, V. Gkinis, C. Holme, R. W. Jacobel, N. B. Karlsson, B. A. Keisling, S. Kipfstuhl, H. A. Kjær, M. E. L. Kristensen, A. Muto, L. E. Peters, T. Popp, K. L. Riverman, A. M. Svensson, C. Tibuleac, B. M. Vinther, Y. Weng, M. Winstrup, Initial results from geophysical surveys and shallow coring of the Northeast Greenland Ice Stream (NEGIS). *Cryosphere* **8**, 1275–1287 (2014). doi:10.5194/tc-8-1275-2014
59. S. O. Rasmussen, M. Bigler, S. P. Blockley, T. Blunier, S. L. Buchardt, H. B. Clausen, I. Cvijanovic, D. Dahl-Jensen, S. J. Johnsen, H. Fischer, V. Gkinis, M. Guillevic, W. Z. Hoek, J. J. Lowe, J. B. Pedro, T. Popp, I. K. Seierstad, J. P. Steffensen, A. M. Svensson, P. Vallelonga, B. M. Vinther, M. J. C. Walker, J. J. Wheatley, M. Winstrup, A stratigraphic framework for abrupt climatic changes during the Last Glacial period based on three synchronized Greenland ice-core records: Refining and extending the INTIMATE event stratigraphy. *Quat. Sci. Rev.* **106**, 14–28 (2014). doi:10.1016/j.quascirev.2014.09.007
60. E. Cook, P. M. Abbott, N. J. G. Pearce, S. Mojtabavi, A. Svensson, A. J. Bourne, S. O. Rasmussen, I. K. Seierstad, B. M. Vinther, J. Harrison, E. Street, J. P. Steffensen, F. Wilhelms, S. M. Davies, Volcanism and the Greenland ice cores: A new tephrochronological framework for the last glacial-interglacial transition (LGIT) based on cryptotephra deposits in three ice cores. *Quat. Sci. Rev.* **292**, 107596 (2022). doi:10.1016/j.quascirev.2022.107596
61. C. Hayward, High spatial resolution electron probe microanalysis of tephras and melt inclusions without beam-induced chemical modification. *Holocene* **22**, 119–125 (2012). doi:10.1177/0959683611409777
62. R. Le Maitre *et al*., Eds., *Igneous Rocks. A Classification and Glossary of Terms: Recommendations of the International Union of Geological Sciences Subcommission on the Systematics of Igneous Rocks* (Cambridge University Press, ed. 2, 2002).
63. C. M. Zdanowicz, G. A. Zielinski, M. S. Germani, Mount Mazama eruption: Calendrical age verified and atmospheric impact assessed. *Geology* **27**, 621 (1999). doi:10.1130/0091-7613(1999)027<0621:MMECAV>2.3.CO;2
64. S. Davies, P. G. Albert, A. J. Bourne, S. Owen, A. Svensson, M. S. M. Bolton, E. Cook, B. J. L. Jensen, G. Jones, V. V. Ponomareva, T. Suzuki, Exploiting the Greenland volcanic ash repository to date caldera-forming eruptions and widespread isochrons during the Holocene. *Quat. Sci. Rev.* **334**, 108707 (2024). doi:10.1016/j.quascirev.2024.108707
65. H. Buckland, K. Cashman, S. Engwell, A. Rust, Sources of uncertainty in the Mazama isopachs and the implications for interpreting distal tephra deposits from large magnitude eruptions. *Bull. Volcanol.* **82**, 23 (2020). doi:10.1007/s00445-020-1362-1
66. S. Pyne-O'Donnell, P. D. M. Hughes, D. G. Froese, B. J. L. Jensen, S. C. Kuehn, G. Mallon, M. J. Amesbury, D. J. Charman, T. J. Daley, N. J. Loader, D. Mauquoy, F. A. Street-Perrott, J. Woodman-Ralph, High-precision ultra-distal Holocene tephrochronology in North America. *Quat. Sci. Rev.* **52**, 6–11 (2012). doi:10.1016/j.quascirev.2012.07.024
67. B. J. L. Jensen, A. B. Beaudoin, M. A. Clynne, J. Harvey, J. W. Vallance, A re-examination of the three most prominent Holocene tephra deposits in western Canada: Bridge River, Mount St. Helens Yn and Mazama. *Quat. Int.* **500**, 83–95 (2019). doi:10.1016/j.quaint.2019.03.017
68. M. Brader, J. M. Lloyd, N. L. M. Barlow, H. Norðdahl, M. J. Bentley, A. J. Newton, Postglacial relative sea-level changes in northwest Iceland: Evidence from isolation basins, coastal lowlands and raised shorelines. *Quat. Sci. Rev.* **169**, 114–130 (2017). doi:10.1016/j.quascirev.2017.05.022
69. G. A. Zielinski, P. A. Mayewski, L. D. Meeker, K. Grönvold, M. S. Germani, S. Whitlow, M. S. Twickler, K. Taylor, Volcanic aerosol records and tephrochronology of the Summit, Greenland, ice cores. *J. Geophys. Res.* **102** (C12), 26625–26640 (1997). doi:10.1029/96JC03547
70. P. A. Mayewski, L. D. Meeker, M. S. Twickler, S. Whitlow, Q. Yang, W. B. Lyons, M. Prentice, Major features and forcing of high-latitude northern hemisphere atmospheric circulation using a 110,000-year-long glaciochemical series. *J. Geophys. Res.* **102** (C12), 26345–26366 (1997). doi:10.1029/96JC03365
71. I. K. Seierstad, P. M. Abbott, M. Bigler, T. Blunier, A. J. Bourne, E. Brook, S. L. Buchardt, C. Buizert, H. B. Clausen, E. Cook, D. Dahl-Jensen, S. M. Davies, M. Guillevic, S. J. Johnsen, D. S. Pedersen, T. J. Popp, S. O. Rasmussen, J. P. Severinghaus, A. Svensson, B. M. Vinther, Consistently dated records from the Greenland GRIP, GISP2 and NGRIP ice cores for the past 104 ka reveal regional millennial-scale δ18O gradients with possible Heinrich event imprint. *Quat. Sci. Rev.* **106**, 29–46 (2014). doi:10.1016/j.quascirev.2014.10.032
72. J. Lin, A. Svensson, C. S. Hvidberg, J. Lohmann, S. Kristiansen, D. Dahl-Jensen, J. P. Steffensen, S. O. Rasmussen, E. Cook, H. A. Kjær, B. M. Vinther, H. Fischer, T. Stocker, M. Sigl, M. Bigler, M. Severi, R. Traversi, R. Mulvaney, Magnitude, frequency and climate forcing of global volcanism during the last glacial period as seen in Greenland and Antarctic ice cores (60–9 ka). *Clim. Past* **18**, 485–506 (2022). doi:10.5194/cp-18-485-2022
73. B. L. N. Kennett, *The seismic wavefield I. Introduction and theoretical development* (Cambridge University Press, 2001).
74. S. Chaisri, E. S. Krebes, Exact and approximate formulas for *P - SV* reflection and transmission coefficients for a nonwelded contact interface. *J. Geophys. Res.* **105** (B12), 28045–28054 (2000). doi:10.1029/2000JB900296
75. E. M. Schulson, S. T. Nodder, C. E. Renshaw, On the restoration of strength through stress-driven healing of faults in ice. *Acta Mater.* **117**, 306–310 (2016). doi:10.1016/j.actamat.2016.06.046

76. M. V. Afanasiev, C. Boehm, M. van Driel, L. Krischer, M. Rietmann, D. A. May, M. G. Knepley, A. Fichtner, Modular and flexible spectral-element waveform modelling in two and three dimensions. *Geophys. J. Int.* **216**, 1675–1692 (2019). doi:10.1093/gji/ggy469
77. A. Fichtner, C. Hofstede, B. L. N. Kennett, N. F. Nymand, M. L. Lauritzen, D. Zigone, O. Eisen, Fiber-optic airplane seismology on the Northeast Greenland Ice Stream. *Seismic Record* **3**, 125–133 (2023). doi:10.1785/0320230004
78. H. Kohnen, *Zeitschrift f* (Geophysik, 1972), pp. 925–935.
79. S. G. Sheldon, J. P. Steffensen, S. B. Hansen, T. J. Popp, S. J. Johnsen, The investigation and experience of using ESTISOL™ 240 and COASOL™ for ice-core drilling. *Ann. Glaciol.* **55**, 219–232 (2014). doi:10.3189/2014AoG68A036
80. E. Fjær, R. M. Holt, P. Horsrud, A. M. Raaen, R. Risnes, Eds., *Petroleum Related Rock Mechanics*, vol. 33 of *Developments in Petroleum Science* (Elsevier, 1992), pp. 109–134.
81. A. Løkkegaard, K. D. Mankoff, C. Zdanowicz, G. D. Clow, M. P. Lüthi, S. H. Doyle, H. H. Thomsen, D. Fisher, J. Harper, A. Aschwanden, B. M. Vinther, D. Dahl-Jensen, H. Zekollari, T. Meierbachtol, I. McDowell, N. Humphrey, A. Solgaard, N. B. Karlsson, S. A. Khan, B. Hills, R. Law, B. Hubbard, P. Christoffersen, M. Jacquemart, J. Seguinot, R. S. Fausto, W. T. Colgan, Greenland and Canadian Arctic ice temperature profiles database. *Cryosphere* **17**, 3829–3845 (2023). doi:10.5194/tc-17-3829-2023

ACKNOWLEDGMENTS

We gratefully acknowledge the careful and constructive comments of four anonymous reviewers who helped us to sharpen our line of arguments. Our experiment would not have been possible without the immense technical support by Søren Børsting, Sverrir Hilmarson and Dorthe-Dahl Jensen. Invaluable technical support, before and during the experiment, was provided by Silixa (Athena Chalari and support team) and Solifos (Andrea Fasciati). We gratefully acknowledge valuable discussions with Richard Alley, Dorthe Dahl-Jensen, Trine Dahl-Jensen, Stewart Fishwick, Thomas Hudson, Brad Lipovsky, Roman Pevzner, Helene Seroussi and Lucas Zoet. **Funding:** Olaf Eisen and Dimitri Zigone were supported by the CHIPSM grant of the University of Strasbourg Institute for Advanced Studies and by the French Europe & Foreign Affair ministry and the French Higher Education and Research ministry under the project number 49360YJ - PHC PROCOPE 2023. EastGRIP is directed and organized by the Centre for Ice and Climate at the Niels Bohr Institute, University of Copenhagen. It is supported by funding agencies and institutions in Denmark (A. P. Moller Foundation, University of Copenhagen), the United States (US National Science Foundation, Office of Polar Programs), Germany (Alfred Wegener Institute, Helmholtz Centre for Polar and Marine Research), Japan (National Institute of Polar Research and Arctic Challenge for Sustainability), Norway (University of Bergen and Trond Mohn Foundation), Switzerland (Swiss National Science Foundation), France (French Polar Institute Paul-Emile Victor, Institute for Geosciences and Environmental Research), Canada (University of Manitoba) and China (Chinese Academy of Sciences and Beijing Normal University). **Author contributions**: Fichtner: data acquisition, formal data analysis, interpretation; Hofstede: data acquisition, interpretation; Kennett: formal data analysis; Svensson, Westhoff, Ampuero, Cook, Zigone, Jansen, Eisen: interpretation of results and linkage to non-seismic data; Walter: formal data analysis and interpretation. All authors contributed to writing and revision. **Competing interests**: None of the authors declares any competing interests. **Data and materials availability**: All data presented in this paper, as well as Python code to read and visualize them, is available on Zenodo: https://doi.org/10.5281/zenodo.14811755.

SUPPLEMENTARY MATERIALS

science.org/doi/10.1126/science.adp8094
Materials and Methods
Supplementary Text
Figs. S1 to S21
References (*60–81*)

Submitted 17 April 2024; accepted 21 January 2025
Published online 6 February 2025
10.1126/science.adp8094

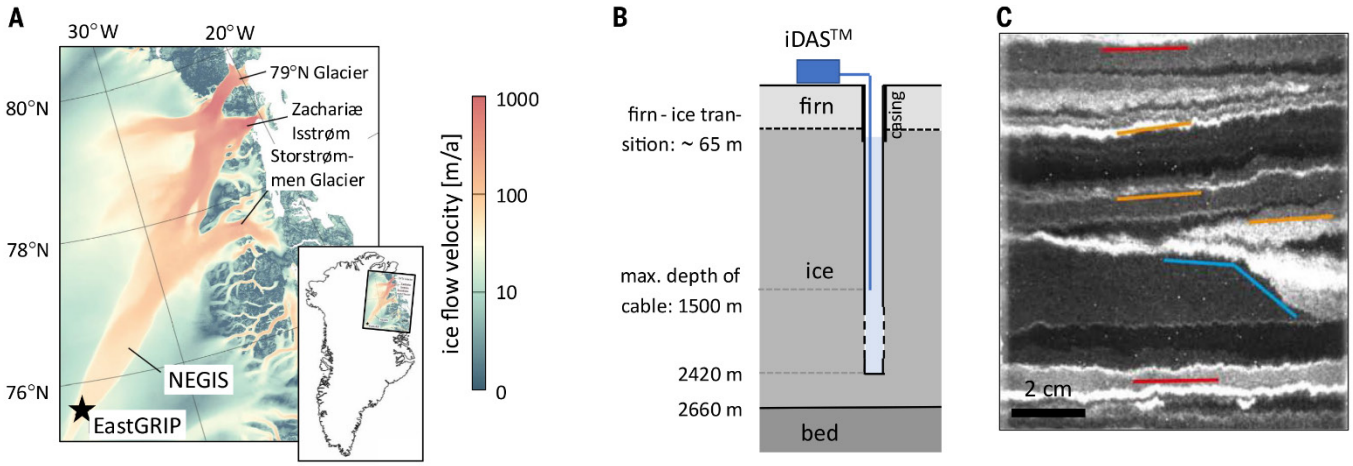

Fig. 1. Experimental setting. (**A**) The Northeast Greenland Ice Stream (NEGIS) and its outlet glaciers shown in the form of surface flow velocities (*41*). (**B**) Schematic, not-to-scale illustration of the experimental setup. The DAS cable, shown as blue line, reached a maximum depth of 1500 m inside the 2420 m deep borehole within the 2660 m deep ice (*58*). A Silixa iDAS™ v2 interrogator was used to perform measurements at 1 kHz sampling rate and with 1 m channel spacing. (**C**) Optical line scan image of a structure similar to geological thrust faults, yet only partly visible due to the narrow diameter of the ice core. The sample is from 1690.65 m depth. Colored lines indicate the ramp (in blue), general layering of the section (red), and changed layer tilt inside the structure (orange). Figure modified from (*15*).

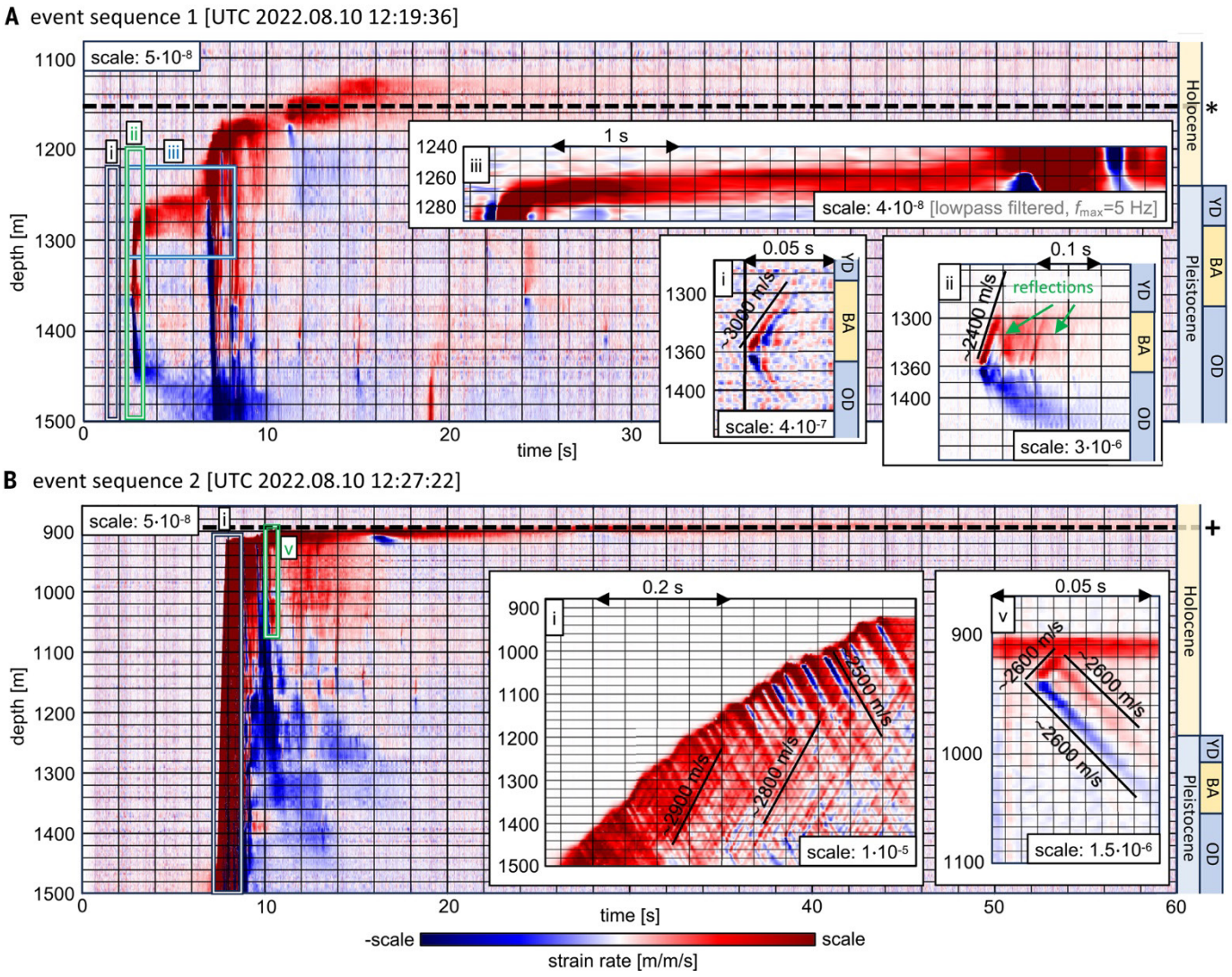

Fig. 2. DAS recordings of seismic events. Sequences 1 (**A**) and 2 (**B**) are shown, with ∗ marking the depth of the Saksunarvatn tephra (Grimsvötn) dated at 10.2 ka b2k, and + marking the depth of the Mt. Mazama tephra (Crater Lake) dated at 7.6 ka b2k. (See section S3.1 for details.) Here and in all subsequent figures, positive strain rates correspond to extension along the cable, and and negative ones to shortening. Values for the color scale ranges are provided in the subfigures. For notational consistency, selected close-ups are labeled in the same way as figs. S1 and S2. (For instance, close-ups/subevents ii to iv for sequence 2 not shown here are shown in fig. S2.) Abbreviations in the geologic time scales to the right have the following meaning: YD: Younger Dryas/GS-1 stadial, BA: Bølling-Allerød/GI-1 interstadial, OD: Oldest Dryas/GS-2 stadial (*59*).

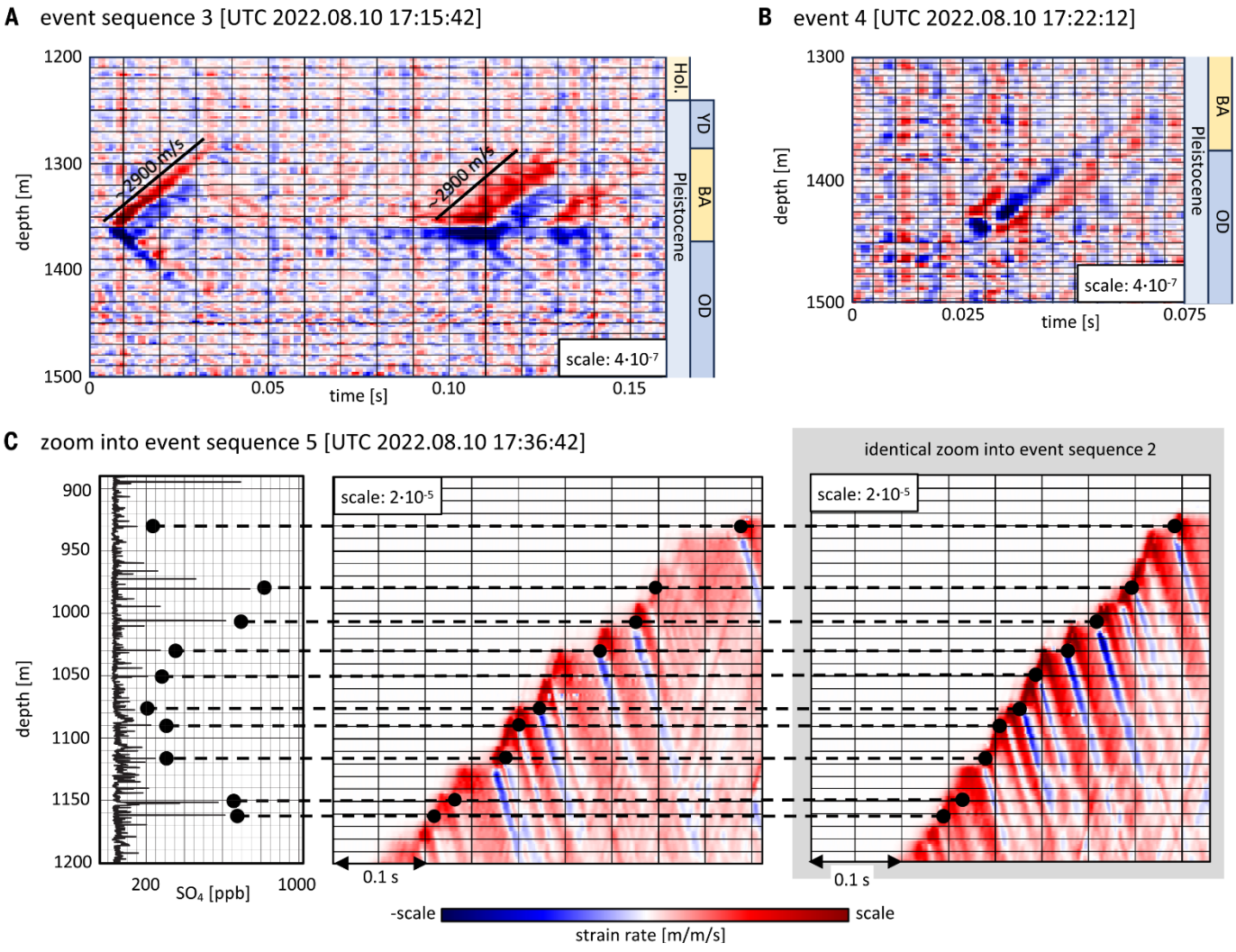

Fig. 3. DAS recordings of seismic events. Shown are sequence 3 (**A**), the isolated event 4 (**B**), and part of event sequence 5 (**C**), which is nearly identical to sequence 2. For comparison of sequences 2 and 5, close-up views of both are shown next to each other. The initiation depths of subevents closely correspond to SO_4 peaks, displayed on the left. SO_4 was not measured on the EastGRIP core but was projected onto the EastGRIP depth scale from the GRIP2 dataset, as detailed in supplementary section S3.2. Abbreviations in the geologic time scales are the same as in Fig. 2.

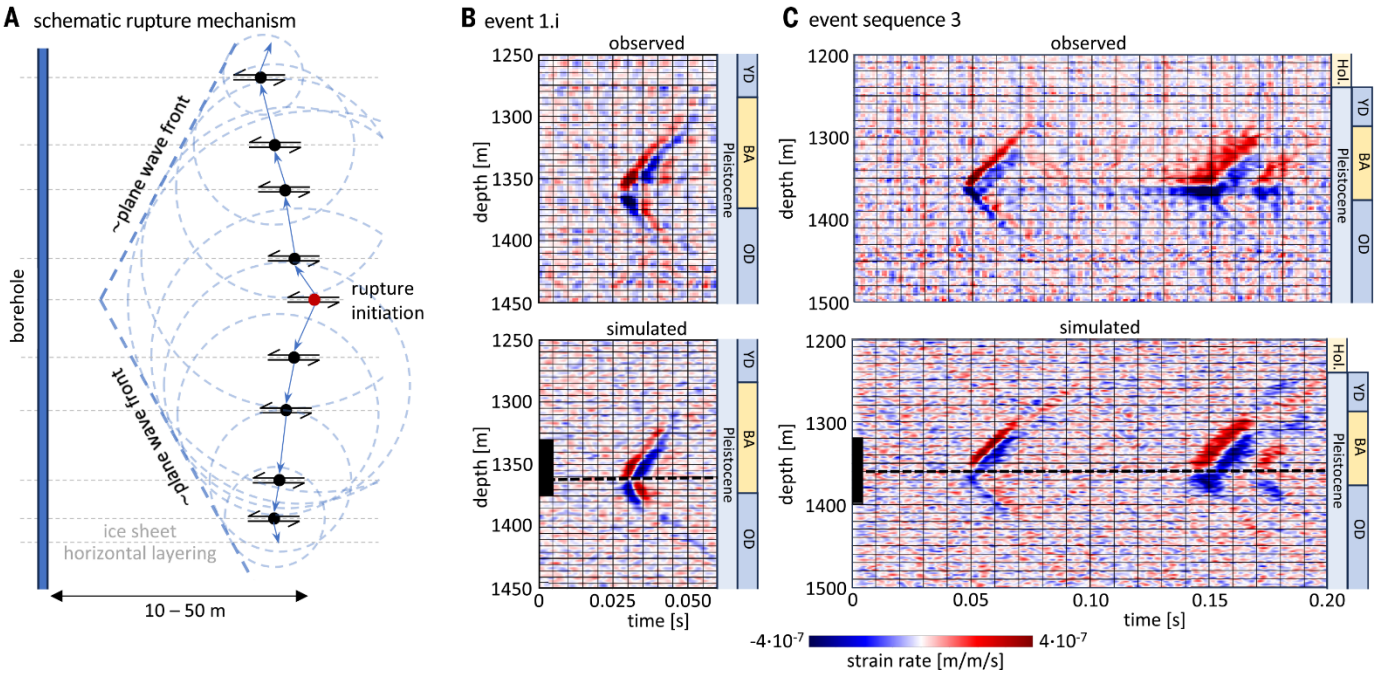

Fig. 4. Comparison of observed and simulated DAS data. (**A**) Cartoon illustration of a vertically oriented array of slip planes. Though their orientation cannot be inferred from the DAS data, they are drawn horizontally for simplicity. The red circle marks the initiation point, from which subsequent ruptures are triggered in up- and downward directions. The superposition of circular wave fronts from the individual ruptures approximately produces a plane wave. (**B** and **C**) Observed (top) and simulated (bottom) DAS recordings of event 1.i and event sequence 3. For a more realistic comparison, we added bandpass filtered Gaussian noise to the simulations. The black bar in the simulation panels marks the depth extent of the vertically oriented horizontal slip array, and the black dashed lines indicates the initiation depth. The exact moment density distributions used in the simulations are shown in figs. S14 and S16. For both event 1.i and sequence 3, the source array falls into the Bølling-Allerød/GI-1 depth range, characterized by climatically warmer and more viscous ice. Geologic time scale abbreviations as in Fig. 2.

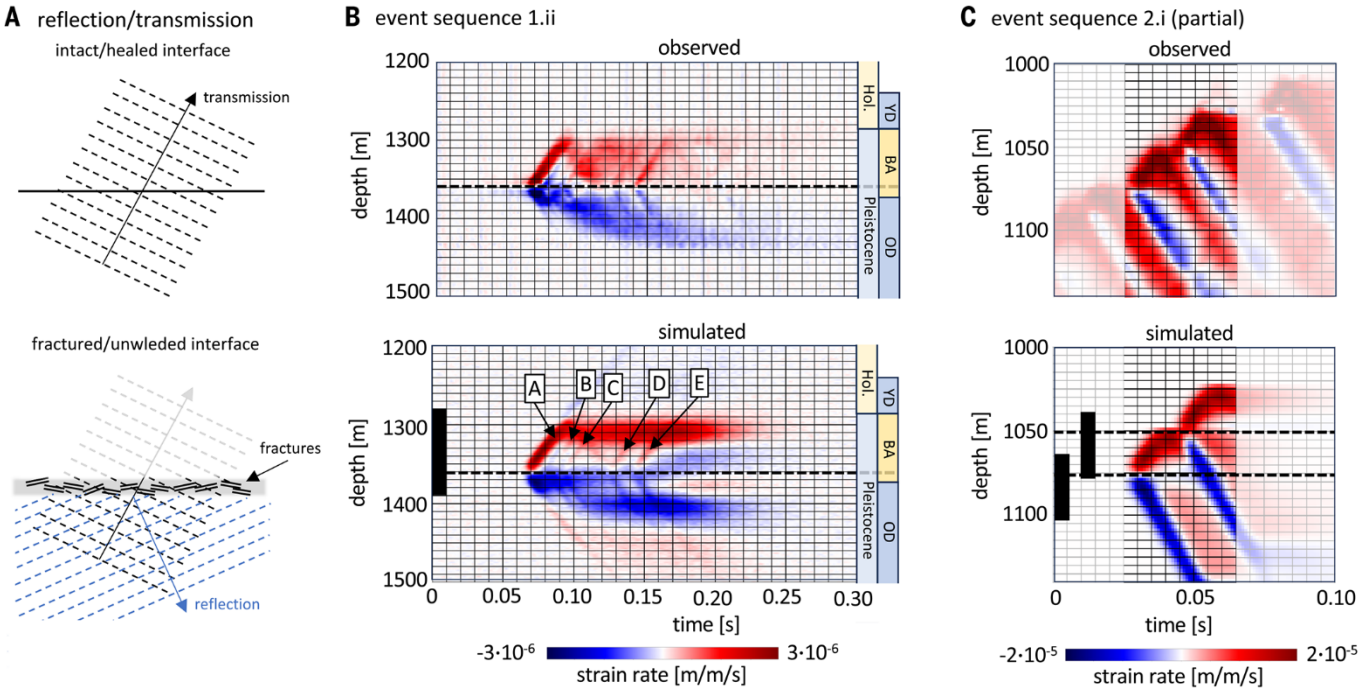

Fig. 5. Comparison of observed and simulated sequences. Shown are sequences 1.ii (B) and 2.i (C). (A) Cartoon illustration of wave transmission and reflection at intact/healed (top) and fractured/unwelded (bottom) interfaces. and (C) Similar to Fig. 4, the black bars mark the depth extent of the vertically oriented horizontal slip array, and the black dashed lines indicate the rupture initiation depths. The exact moment density distributions used in the simulations are shown in figs. S17 and S16. The five subevents used to model sequence 1.ii are labeled A to E. As for events 1.i and 3, the source array of sequence 1.ii falls into the Bølling-Allerød/GI-1 depth range. Geologic time scale abbreviations as in Fig. 2.